Supporting Information for

Chaos-Generating Periodic Orbits of Topological Defects in Confined Active Nematics

Brandon Klein, Alejandro J. Soto Franco, Md Mainul Hasan Sabbir, Matthew J. Deutsch, Ross Kliegman, Robin L. B. Selinger, Kevin A. Mitchell, Daniel A. Beller

Daniel A. Beller
E-mail: d.a.beller@jhu.edu

This PDF file includes:

Other supporting materials for this manuscript include the following:

Movies S1 to S10

Supporting Information Text

Numerical methods

Nematohydrodynamics .

Pressure field. In the incompressible Navier-Stokes equations 12, 13, the pressure field, p, plays the exclusive role of maintaining Eq. 13. This is achieved in our numerical implementation by taking the divergence of Eq. 12 and solving the standard pressure-Poisson scheme (1), keeping terms up to second order in derivatives of $\mathbf{u}$:

$$\nabla^2 p = -\nabla\cdot(\mathbf{u}\cdot\nabla)\mathbf{u} + \nabla\cdot\frac{1}{\rho}\mathbf{F} - \nabla\cdot\partial_t\mathbf{u}|_t \qquad \text{[SI.1]}$$

with a Laplacian stencil of p, such that $\nabla\cdot\partial_t\mathbf{u}|_{t+\delta t} = 0$.

We integrate equations 8 and 10 forward in time with a time step of $\delta t = 1\text{e}{-4}$ using the Euler method (2). Advection terms for $\mathbf{u}$ and Q_{ij} are calculated using an upwind scheme which computes advection coming from the direction of the local flow field (3).

Boundary conditions. To simulate strong tangential anchoring on an arbitrarily curved boundary with local unit tangent $\hat{\tau}$, we apply Dirichlet conditions on the nematic domain Ω, with boundary $\partial\Omega$. Specifically,

$$\begin{pmatrix} Q_{xx} \\ Q_{xy} \end{pmatrix}\Bigg|_{\partial\Omega}(\mathbf{r}) = S\begin{pmatrix} \tau_x^2 - 1/2 \\ \tau_x\tau_y \end{pmatrix}. \qquad \text{[SI.2]}$$

In order to provide the force from such a boundary that would result in this anchoring, or equivalently that $\partial_t Q_{ij} = 0$, we set the molecular field along $\partial\Omega$ based on equation 8 as

$$H_{ij}\Big|_{\partial\Omega} = \gamma[u_k\partial_k Q_{ij} - \chi S E_{ij} + [\omega, Q] + 2\mathrm{Tr}[QE]Q_{ij}]. \qquad \text{[SI.3]}$$

For the flow velocity field, we use a no-slip boundary condition, $\mathbf{u}\big|_{\partial\Omega} = 0$. Equation SI.1 is an instance of Poisson's equation, which has a unique solution so long as Neumann or Dirichlet boundary conditions are defined. To do this, we consider that there are no outflows or inflows along the boundary, $\hat{\nu}\cdot\mathbf{u}\big|_{\partial\Omega} = 0$, and derive a Neumann boundary condition using $\hat{\nu}\cdot\partial_t\mathbf{u}\big|_{\partial\Omega} = 0$, with $\hat{\nu}$ being the outward-pointing unit normal to the boundary and with

$$\hat{\nu}\cdot\partial_t\mathbf{u}\big|_{\partial\Omega} = \hat{\nu}\cdot\left[-(\mathbf{u}\cdot\nabla)\mathbf{u} + \eta\nabla^2\mathbf{u} + \frac{1}{\rho}\mathbf{F} - \frac{1}{\rho}\nabla p\right]\Bigg|_{\partial\Omega}. \qquad \text{[SI.4]}$$

Upon applying the no-flux condition at the boundary, $\hat{\nu}\cdot\mathbf{u}|_{\partial\Omega} = 0$, and the corollary that the tangential derivative of the normal component of velocity must vanish, $\partial_\tau(\hat{\nu}\cdot\mathbf{u}) = 0|_{\partial\Omega}$, we obtain the following Neumann condition for the normal derivative of the pressure at the boundary:

$$\partial_\nu p\big|_{\partial\Omega} = \left(\rho\eta\nabla^2 u_\nu + F_\nu\right)|_{\partial\Omega}. \qquad \text{[SI.5]}$$

Note that $u_\nu\big|_{\partial\Omega} = 0$ even if there is slipping, which necessarily occurs along $\hat{\tau}$. Importantly, our scheme is generalizable to $\mathcal{C}^1$-continuous curves.

For compatibility with our finite differencing scheme, we need to regularize the cusps of the epicycloids into $\mathcal{C}^1$-continuous curves, which also enables us to model the smoothness of the "cusp" in the experiments of Ref. (4) at the scale of the microtubule bundles. For this purpose, we use as our family of boundary surfaces the epitrochoids defined parametrically by

$$\begin{aligned} x(u) &= \frac{r}{2q}\left[(2q-1)\cos(u) + d\cos((2q-1)u)\right] \\ y(u) &= \frac{r}{2q}\left[(2q-1)\sin(u) + d\sin((2q-1)u)\right] \\ &\qquad\qquad u \in [0, 2\pi), \end{aligned} \qquad \text{[SI.6]}$$

where the new parameter d varies between 0 and 1 continuously interpolates between a circle and the epicycloids. These represent paths tracing a point on a circle of radius r at distance $r\cdot d$ from its center as it rolls on the circumference of a circle R. We use $d = 0.99$ to approximate the epicycloids near their sharp limit.

A. Time averaged vorticity on epicycloid simulations. Our theoretical framework predicts that the number of gyres in the time averaged vorticity only depends on boundary topology, not geometry. We show that the epicycloid simulations performed agree with our analytical prediction, by showing the time averaged vorticity as a function of space for the braiding regimes discussed in Figure 7 of the main text.

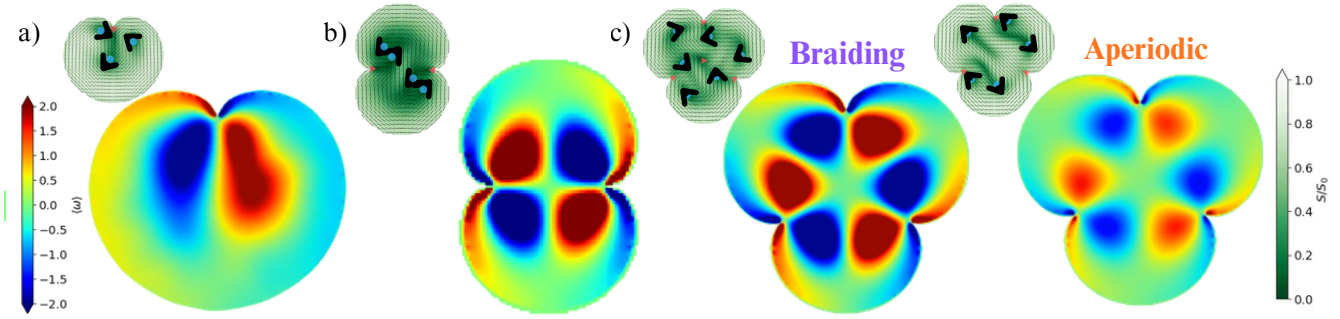

Fig. S1. (a), (b), and (c) show the time averaged vorticity after 1.5×10^6 time-steps for the braiding and aperiodic regimes in the cardioid, nephroid, and trefoiloid. Insets show the corresponding snapshots from Figure 7 (a), (c), and (e).

Agent-based model . The three-dimensional coarse-grained dynamical simulations represent active microtubules as bead-spring chain filaments, confined within a volume defined by a cardioid-shaped area with a small thickness, $L = 3.2\sigma$, in the vertical direction. Interactions between beads are represented by a short-range, repulsive, Weeks-Chandler-Anderson interaction with an additional short-range attractive depletion force:

$$U(r) = \begin{cases} 4\varepsilon\left[\left(\frac{\sigma}{r}\right)^{12} - \left(\frac{\sigma}{r}\right)^{6}\right] + f_{\text{dep}} r, & \text{if } r < 2^{\frac{1}{6}}\sigma, \\ 0, & \text{if } r \geq 2^{\frac{1}{6}}\sigma. \end{cases} \quad \text{[SI.7]}$$

The bead-bead interaction has parameters of $\varepsilon = 0.5$, $\sigma = 1.0$, and the additional depletion force is $\mathbf{f}_{\text{dep}} = 0.25$. Bonded interactions between adjacent beads on each chain are represented as linear elastic springs with potential:

$$U_{\text{bond}}(r) = \frac{k_1}{2}(r - l_0)^2 \quad \text{[SI.8]}$$

where l_0 is the equilibrium length of the spring and k_1 is the spring constant. Bond-bending terms are represented by second- and third-neighbor linear spring interactions with spring constants k_2 and k_3 and equilibrium lengths $2l_0$ and $3l_0$:

$$U_{\text{bend}} = \frac{k_2}{2}(|\mathbf{r}_{i+2} - \mathbf{r}_i| - 2l_0)^2 + \frac{k_3}{2}(|\mathbf{r}_{i+3} - \mathbf{r}_i| - 3l_0)^2 \quad \text{[SI.9]}$$

In Eq. SI.8 and Eq. SI.9 equilibrium length, $l_0 = 0.8$, bond spring constant, $k_1 = 57.1464$, and bend spring constants $k_2 = k_3 = 50k_1$. The equations of motion for the beads, with mass $m = 1$, are integrated using the Velocity Verlet algorithm.

Extensile activity is modeled via a pairwise active force between beads i and j on adjacent filaments with anti-polar alignment, of the form:

$$\mathbf{F}_i = \alpha \frac{\frac{1}{2}(\hat{t}_i - \hat{t}_j)}{|\mathbf{r}_{ij}|}, \qquad \mathbf{F}_j = -\mathbf{F}_i, \quad \text{[SI.10]}$$

where $\hat{t}$ is the tangent vector of the adjacent filaments at the positions of beads i and j and activity parameter, $\alpha = 0.06$. We note that this active filament activity parameter, α, does not map to the nematohydrodynamic activity, ζ. We add a constant short-range attractive force, $\mathbf{f}_{\text{attract}}$, to the pairwise active force to represent the attractive pull of kinesin motor proteins on two adjacent filaments undergoing shear. Activity is only applied to adjacent filaments if $\hat{t}_i \cdot \hat{t}_j \leq 0.5$, resulting in extensile activity through inter-filament shear. Our coarse-grained model assumes that there is a uniform, high density, of kinesin motor proteins and adenosine triphosphate chemical energy (ATP). The model thus does not show the characteristic slowing of extensile shear as ATP density drops with time as seen in experiment (5).

To enable long-range hydrodynamic interactions, we introduce a coarse-grained two-dimensional fluid layer located below the filament volume and coupled to the filaments. This novel underlying fluid layer is introduced for two effects: to thermostat the active matter, and to provide long-range hydrodynamic interactions across areas with low active filament density. Fluid-fluid particle interactions are governed by a short-range, repulsive, Weeks-Chandler-Anderson potential similar to Eq. SI.7. Fluid particles are thermostatted by a pairwise dissipative particle dynamics thermostat (6). Interactions between fluid particles and active particles are represented by a Lennard-Jones interaction with interaction strength mediated by an artificial distance offset between the fluid layer and the active layer. This interaction puts all active particles in the simulation volume in contact with the fluid thermostat.

Arbitrarily shaped boundary conditions can be imposed on both active and fluid particles in the system by generating a wall of immobile boundary particles which have an exclusively repulsive soft-sphere potential interaction. For the single-cusp cardioid system the boundary particles were laid out with the epicycloid equations for $q = 3/2$,where $r = 123\sigma$ is the characteristic radius of the cardioid and u is calculated to produce equally-spaced boundary particles along the perimeter of the cardioid. The spacing between boundary particles is calculated to give a uniform repulsive force along the boundary and to be small enough to effectively confine the fluid and active particles.

Analytical methods

The Artin braid group and topological entropy. The Artin braid groups are closed under a product operation. The Burau representation is given by (7)

$$(\sigma_i)_{kl} = \delta_{kl} + \delta_{i-1,k}\delta_{il} - \delta_{i+1,k}\delta_{il},$$
$$(\sigma_i^{-1})_{kl} = \delta_{kl} - \delta_{i-1,k}\delta_{il} + \delta_{i+1,k}\delta_{il}. \quad [1]$$

and consists of $2(n-1)$ matrices of size $(n-1)\times(n-1)$ where the empty product and group identity is mapped to the $n-1$ dimensional identity matrix. This matrix representation is constructed to maintain the Artin group relations: $[\sigma_i, \sigma_j] = 0$ if $|i-j| > 1$, and $\sigma_i\sigma_{i+1}\sigma_i = \sigma_{i+1}\sigma_i\sigma_{i+1}$. Importantly, this means that a braidword can be represented as a matrix product, and that a periodic steady state corresponds to the application of β^{n_c} for n_c cycles. In the large-n_c limit, the matrix product β^{n_c} in its eigenbasis is dominated by its largest-magnitude eigenvalue $b_{\max}^{n_c}$, where $b_{\max}$ is the largest eigenvalue of β. Because the defects, as stirring rods, drag the fluid with them, the minimal stretching of material contours required to accommodate the described defect braiding grows with n_c as $b_{\max}^{n_c}$. The topological entropy therefore grows linearly with n_c, as $h \cdot t \sim \log(|b_{\max}^{n_c}|) = n_c \log(|b_{\max}|)$. Since n_c is proportional to time for periodic braiding, h is proportional to $\log(|b_{\max}|)$. Note that, if the motion is periodic, h is independent of the projection used.

Burau representation of $\mathbf{B}_3$ and $\mathbf{B}_4$. The elements of $\mathbf{B}_3$ in the Burau representation are

$$\sigma_1 = \begin{pmatrix} 1 & 1 \\ 0 & 1 \end{pmatrix},\ \sigma_1^{-1} = \begin{pmatrix} 1 & -1 \\ 0 & 1 \end{pmatrix},$$
$$\sigma_2 = \begin{pmatrix} 1 & 0 \\ -1 & 1 \end{pmatrix},\ \sigma_2^{-1} = \begin{pmatrix} 1 & 0 \\ 1 & 1 \end{pmatrix}. \quad [SI.11]$$

An iteration of the golden braid then looks like

$$\beta_{\text{golden}} = \sigma_2^{-1}\sigma_1 = \begin{pmatrix} 1 & 0 \\ 1 & 1 \end{pmatrix}\begin{pmatrix} 1 & 1 \\ 0 & 1 \end{pmatrix} = \begin{pmatrix} 1 & 1 \\ 1 & 2 \end{pmatrix}. \quad [SI.12]$$

The eigenvalues of this matrix are $\frac{3+\sqrt{5}}{2} = 1+\phi_0 = \phi_0^2$, and $\frac{3-\sqrt{5}}{2} = 1-(\phi_0-1) = (\phi_0-1)^2$, where $\phi_0 = \frac{1+\sqrt{5}}{2}$ is the golden ratio. Another method to see the rate of stretching is to consider the action of this braidword on an arbitrary vector $\begin{pmatrix} x \\ y \end{pmatrix}$, which gives

$$\begin{pmatrix} x' \\ y' \end{pmatrix} = \beta_{\text{golden}}\begin{pmatrix} x \\ y \end{pmatrix} = \begin{pmatrix} 1 & 1 \\ 1 & 2 \end{pmatrix}\begin{pmatrix} x \\ y \end{pmatrix}$$
$$= \begin{pmatrix} x+y \\ x+2y \end{pmatrix}. \quad [SI.13]$$

Let F_k be the k^{th} Fibonacci number. It holds that if $x = F_{n-2}$, and $y = F_{n-1}$, then

$$x' = F_{n-1} + F_{n-2} = F_n, \quad [SI.14]$$

and

$$y' = 2F_{n-1} + F_{n-2} = F_n + F_{n-1} = F_{n+1}. \quad [SI.15]$$

Thus, by induction, powers of β_{golden} produce the Fibonacci sequence.

The elements of $\mathbf{B}_4$ are given as

$$\sigma_1 = \begin{pmatrix} 1 & 0 & 0 \\ -1 & 1 & 0 \\ 0 & 0 & 1 \end{pmatrix},\ \sigma_1^{-1} = \begin{pmatrix} 1 & 0 & 0 \\ 1 & 1 & 0 \\ 0 & 0 & 1 \end{pmatrix},$$
$$\sigma_2 = \begin{pmatrix} 1 & 1 & 0 \\ 0 & 1 & 0 \\ 0 & -1 & 1 \end{pmatrix},\ \sigma_2^{-1} = \begin{pmatrix} 1 & -1 & 0 \\ 0 & 1 & 0 \\ 0 & 1 & 1 \end{pmatrix}, \quad [SI.16]$$
$$\sigma_3 = \begin{pmatrix} 1 & 0 & 0 \\ 0 & 1 & 1 \\ 0 & 0 & 1 \end{pmatrix},\ \sigma_3^{-1} = \begin{pmatrix} 1 & 0 & 0 \\ 0 & 1 & -1 \\ 0 & 0 & 1 \end{pmatrix}.$$

An iteration of the silver braid, $\sigma_3\sigma_1\sigma_2\sigma_3^{-1}\sigma_1^{-1}\sigma_2^{-1}$, then looks like

$$\begin{aligned}\beta_{\text{silver}} &= \sigma_3\sigma_1\sigma_2\sigma_3^{-1}\sigma_1^{-1}\sigma_2^{-1} \\ &= \begin{pmatrix}1&0&0\\0&1&1\\0&0&1\end{pmatrix}\begin{pmatrix}1&0&0\\-1&1&0\\0&0&1\end{pmatrix} \\ &\quad \begin{pmatrix}1&1&0\\0&1&0\\0&-1&1\end{pmatrix}\begin{pmatrix}1&0&0\\0&1&-1\\0&0&1\end{pmatrix} \\ &\quad \begin{pmatrix}1&0&0\\1&1&0\\0&0&1\end{pmatrix}\begin{pmatrix}1&-1&0\\0&1&0\\0&1&1\end{pmatrix} \\ &= \begin{pmatrix}2&-2&-1\\-2&3&2\\-1&2&2\end{pmatrix}.\end{aligned} \tag{SI.17}$$

The eigenvalues of this matrix are $3+2\sqrt{2} = 1+2\phi_1 = \phi_1^2$, $3-2\sqrt{2} = 1-2(\phi_1-2) = (\phi_1-2)^2$, and $1 = \phi_1(\phi_1-2)$, where $\phi_1 = 1+\sqrt{2}$ is the silver ratio. By definition both the golden and silver ratios obey the conjugate and identity relations of the metallic ratios:

$$\begin{aligned}1 + k\phi_{k-1} &= \phi_{k-1}^2, \\ 1 - k(\phi_{k-1}-k) &= (\phi_{k-1}-k)^2,\end{aligned} \tag{SI.18}$$

and thus,

$$\phi_{k-1}(\phi_{k-1}-k) = 1. \tag{SI.19}$$

Movie S1. Simulation over 3.35×10^5 time-steps of a 100×100 simulation of an active nematic confined to a disk with fixed tangential anchoring. Defect trajectories (blue and green) are shown in the disk on the left. Defect worldlines are displayed on the right. The projection axis denoted "X" is the horizontal axis of the disk.

Movie S2. (0-50 seconds) Simulation over 7.5×10^5 time-steps of a 100×100 simulation of an active nematic confined to a disk with fixed $q=3/2$ anchoring. Defect trajectories (blue, green, and purple) are shown in the disk on the left. Defect worldlines are displayed on the right. The projection axis denoted "X" is the horizontal axis of the disk. (50-66 seconds) Line stretching depicts an advected contour (blue) undergoing exponential stretching due to defect mixing (red). The director outside the circular domain is arbitrarily defined as horizontal and not simulated.

Movie S3. (0-33 seconds) Simulation over 5.0×10^5 time-steps of a 100×100 simulation of an active nematic confined to a disk with fixed q=4/2 anchoring. Defect trajectories (blue, green, and purple) are shown in the disk on the left. Defect worldlines are displayed on the right. The projection axis denoted "X" is the horizontal axis of the disk. (50-49 seconds) Line stretching depicts an advected contour (blue) undergoing exponential stretching due to defect mixing (red). The director outside the circular domain is arbitrarily defined as horizontal and not simulated.

Movie S4. Simulation over 7.5×10^5 time-steps of a 100×100 simulation of an active nematic confined to a disk with fixed $q=3/2$ anchoring. The top three graphs show the instantaneous vorticity, the running time-averaged vorticity, and the running standard deviation of the vorticity. The bottom three graphs show the instantaneous $\mathcal{Q}$-criterion with $\mathcal{Q}=0$ isolines shown in black, the running time-averaged $\mathcal{Q}$-criterion, and the running standard deviation of the $\mathcal{Q}$-criterion.

Movie S5. Simulation over 5×10^5 time-steps of a 100×100 simulation of an active nematic confined to a disk with fixed $q=4/2$ anchoring. The top three graphs show the instantaneous vorticity, the running time-averaged vorticity, and the running standard deviation of the vorticity. The bottom three graphs show the instantaneous $\mathcal{Q}$-criterion with $\mathcal{Q}=0$ isolines shown in black, the running time-averaged $\mathcal{Q}$-criterion, and the running standard deviation of the $\mathcal{Q}$-criterion.

Movie S6. Simulation over 1.3×10^6 time-steps of a 100×100 simulation of an active nematic confined to a disk with fixed $q=5/2$ anchoring. The top three graphs show the instantaneous vorticity, the running time-averaged vorticity, and the running standard deviation of the vorticity. The bottom three graphs show the instantaneous $\mathcal{Q}$-criterion with $\mathcal{Q}=0$ isolines shown in black, the running time-averaged $\mathcal{Q}$-criterion, and the running standard deviation of the $\mathcal{Q}$-criterion.

Movie S7. Representative videos of the active phases seen in Figure 7b. All simulations are performed on a 200×200 lattice for 1.5×10^6 time-steps. (ℓ_a, ℓ_c) values for shown simulations are $(0.0069, 0.0625)$ for turbulent, $(0.0556, 0.0834)$ for arrested, $(0.0417, 0.0486)$ for interrupted (golden), and $(0.0139, 0.0903)$ for golden braid.

Movie S8. Representative videos of the active phases seen in Figure 7d. All simulations are performed on a 100×100 lattice for 1.5×10^6 time-steps. (ℓ_a, ℓ_c) values for shown simulations are $(0.0131, 0.0131)$ for turbulent, $(0.0262, 0.0131)$ for arrested, $(0.0262, 0.0654)$ for interrupted (silver), $(0.0196, 0.0393)$ for mixed interrupted, $(0.0131, 0.1309)$ for melted, and $(0.0131, 0.1178)$ for silver braid.

Movie S9. Representative videos of the active phases seen in Figure 7e. All simulations are performed on a 200×200 lattice for 1.5×10^6 time-steps. (ℓ_a, ℓ_c) values for shown simulations are $(0.0064, 0.0128)$ for turbulent, $(0.0511, 0.0766)$ for arrested, $(0.0192, 0.0766)$ for aperiodic, $(0.0128, 0.0639)$, for interrupted (silver), and $(0.0128, 0.0766)$ for silver braid.

Movie S10. Agent-based simulation in cardioid confinement of 64,000 active particles comprising 800 filaments, each with 80 beads, and an additional 3068 fluid particles. The left shows bead-chain filaments with green indicating CCW polar orientation and orange indicating CW polar orientation with respect to the origin. The right shows locally averaged director field and defect trajectories in blue, green, and red, performing a golden braid cycle.

References

1. TJ Chung, *Computational Fluid Dynamics.* (Cambridge University Press), (2002).
2. B Klein, et al., Chaos-generating-periodic-orbits (https://github.com/Brandonkl/Chaos-Generating-Periodic-Orbits) (2025).
3. R Courant, E Isaacson, M Rees, On the solution of nonlinear hyperbolic differential equations by finite differences. *Commun. on Pure Appl. Math.* **5**, 243–255 (1952).
4. FL Memarian, et al., Controlling chaos: Periodic defect braiding in active nematics confined to a cardioid. *Phys. Rev. Lett.* **132**, 228301 (2024).
5. FL Memarian, et al., Active nematic order and dynamic lane formation of microtubules driven by membrane-bound diffusing motors. *Proc. Natl. Acad. Sci.* **118**, e2117107118 (2021).
6. KP Santo, AV Neimark, Dissipative particle dynamics simulations in colloid and interface science: a review. *Adv. Colloid Interface Sci.* **298**, 102545 (2021).
7. JL Thiffeault, Measuring Topological Chaos. *Phys. Rev. Lett.* **94**, 084502 (2005).